Modelling and optimisation of single-step laser-based gold nanostructure deposition with tunable optical properties

Cian Hughes, Ronán McCann, Julen Eguileor, Komal Bagga, Robert Groarke, Fiona Regan, Dermot Brabazon

Abstract

As nanotechnology has developed the creation of nanostructured surfaces has garnered attention for their application in sensing and catalysis. These are however often expensive, time-consuming, and difficult to produce. In contrast, this investigation is focused on the inexpensive, environmentally friendly and fast technique of Confined Atmospheric Pulsed-laser deposition (CAP). The CAP technique has these advantages because it is an atmospheric, laser-based direct deposition technique.

Herein, the CAP process is examined in an effort to better understand the process and to begin determining the means to control the properties of the nanostructured surfaces produced by varying the laser fluence and the scan strategy during the ablation. During this investigation, a Nd:YAG laser was applied to deposit gold nanostructures directly onto a polymer substrate. The plasmonic properties and morphologies of the surfaces were examined using UV-Vis spectroscopy and Scanning Electron Microscopy (SEM) respectively. A mathematical model was developed to describe the variation of the position and size of the spectral plasmon peaks in response to the sample processing parameters, with the aim of allowing for a degree of control over these properties and gaining some understanding of the mechanism of this deposition process.

1. Introduction

Nanostructured gold surfaces have received much of interest from the research community due to their numerous potential applications, in particular as a functional coating for biosensing [1–5], Surface-Enhanced Raman Spectroscopy (SERS) [6,7] and as catalysts [8,9]. Most nanostructures are currently produced by means of chemical based methods in multiple steps [10], or techniques such as Chemical Vapour Deposition (CVD) [11] or Atomic Layer

Deposition (ALD) [12,13]. However, more recently researchers have reported methods for the direct deposition of nanostructures based on the laser ablation of bulk materials [14]. The ablation of these bulk materials results in an ablation plume from which the desired structures condense and are deposited. Common examples of such methods include Pulsed-Laser Deposition (PLD) [15], Laser-Induced Forward Transfer (LIFT) [16] and Laser-Induced Reverse Transfer (LIRT) [17]. These techniques are often (although, less often in the case of LIRT and LIFT) performed in vacuo, to maximise the lifetime of the ablation plume and allow sufficient time for condensation to occur on the deposition substrate [18]. In addition, LIRT and LIFT require the use of expensive and high maintenance femtosecond lasers, increasing the cost of these fabrication methods [17,18]. The laser-assisted fabrication of nanostructured surfaces has also been achieved by the irradiation of thin-films by the process of dewetting [19–21], whereby a thin metal film on a substrate is rapidly melted and solidifies into a nanostructured feature. Dewetting has the advantage of being able to be performed in atmosphere without the need for the use of a femtosecond laser and offers a high degree of morphological control as its mechanism is extremely well understood and is relatively predictable [22] (especially when compared with other methodologies relying on condensation of nanostructures from plasmas). The process of dewetting does, however, somewhat limit the substrates on which the desired nanostructures can be fabricated, requiring the use of substrates with thicknesses on the order of only a few hundred nanometers [19] and high melting points. Often, this substrate is simply Si and SiO_2 [19–21] although it is also common to see variants of dewetting that require the use of less cost-efficient materials such as c-plane sapphire [23].

Confined Atmospheric PLD (CAP) is a variant of the conventional PLD technique that allows for the deposition of nanostructured metallic thin-films in atmospheric conditions without requiring the use of a femtosecond laser platform [24]. The “confinement” aspect of the CAP method is hypothesised to be its distinguishing feature when compared to conventional PLD. In conventional PLD the quality of a film is generally determined by a Pressure-Distance (PD) scaling law [25], which states that to obtain a film with given properties PD^n must be a constant (where P is ambient pressure, D is the distance between the target and substrate and n is an exponent determined by experimentation). This law arises as a result of the fact that increasing plume pressure increases the rate at which particles in that plume dissipate their energy. During PLD high energy particles are necessary for the

activation of the substrate surface [25], thus if P increases D must decrease to ensure enough high energy particles reach the substrate. In the case of CAP the atmospheric pressure is much higher than the pressure in standard PLD (which is typically performed at pressures of below 75 mTorr). It follows from this that similar results should be obtainable at atmospheric pressure by greatly reducing the distance. The proposed hypothesis for the mechanism of CAP is that by reducing the distance from several centimetres to only a few microns it comes closer to satisfying this PD scaling law in atmospheric conditions. However, depending on the value of n the PD scaling law alone may not entirely be able to account for the deposition observed in the CAP methodology. One possible effect facilitating this process if the PD law alone does not suffice is the effect of spatial confinement on plasma plumes. The confinement of an ablation plume has been shown to increase its lifetime [26], suggesting that confined plasmas retain their electron temperature for longer. As such, it is possible that this confinement effect helps to ensure that the plume retains enough energy to overcome the activation energy of the deposition substrate, thus facilitating deposition. Should this hypothesised mechanism of CAP as a variant of conventional PLD prove true, it would mean that the morphology of the deposited particles could be strongly influenced by controlling the ambient gas, ambient pressure and target-to-substrate distance [33] used during the deposition process, in addition to the parameters examined herein. The CAP methodology results in the direct deposition of structures from bulk metal at a rate of 0.3-2.7mm^2/s by area (in the parameter range tested during this investigation) and as such is a rapid, single step process.

Comparable atmospheric PLD (APLD) techniques performed at greater target-substrate distances (and thus, lacking the “confinement” aspect of CAP) have been reported in many applications, generally requiring a significantly longer deposition time to achieve significant depositions [27,28] requiring, for example, 1800 pulses at 10Hz (i.e. 3 minutes) to deposit a very low density film across a 4mm diameter circular area [27]. Other variants of APLD have been demonstrated avoiding direct deposition from the ejected plume and making use of flowing gases or flowing plasmas to give greater uniformity of particle size and spacing than standard APLD [23]. While this technique compensates for the primary drawback of the atmospheric techniques relative to standard PLD, it does not address the slow deposition rate inherent to most PLD variants that makes them difficult to scale into a process applicable to mass production of nanostructured surfaces. As a result of the relative simplicity and speed of CAP, it is expected that with further study and optimisation this technique has the potential to

be a readily-scalable deposition method that does not require an expensive industrial vacuum setup and can be performed with readily available industrial laser platforms.

To that end, this study utilises a more consistently reproducible version of the CAP methodology than previously described [24] in a study to determine how various deposition parameters influence the optical and morphological properties of the resulting film. The deposition parameters that were examined were selected based on the criteria that they are factors controlled by the laser and galvanometer. Such factors would be the most easily controllable in an industrial environment and thus should result in the derivation of a mathematical model more relevant to a large-scale production process. These parameters were the fluence of the incident laser beam, the speed at which the beam performed its raster scan and the spacing between each raster scanned line in the path the laser followed. The fluence parameter was chosen because this parameter would be expected to have a significant effect on both the energy of the particles in the ejected plasma plume [26] amount of material ablated [15,28]. The scan speed and scan spacing parameters were selected because they determine the amount of spot overlap for successive laser pulses and adjacent scanlines respectively, and as a result they determine the homogeneity of the energy received across the entire scan area [28].

The study described was performed with the future goal in mind of applying the CAP technique to the fabrication of biosensors. This goal informed the decisions made regarding which aspects of the characterisation data obtained should be focused on. Within the UV/Vis spectroscopy data it was decided that particular attention should be given to the examination of the plasmonic features. Tunable plasmonic properties are extremely useful in the optimisation of SERS based [2], Surface Plasmon Resonance (SPR) [4] based and UV/Vis spectroscopy [3] based biosensing platforms. When examining the SEM images obtained it was decided that the primary focus should be upon both the qualitative morphological features of the films and the size of the particles deposited as the morphology [29] and surface area [30] are both key factors in maximising the sensitivity of many biosensing platforms.

2. Materials and Methods

2.1 Materials

ZeonorFilm ZF14-188 (Zeon Chemical L.P. Japan) Cyclic Olefin Polymer (COP) was used as the substrate due to its flexibility and high transparency in the UV-NIR range. A 10 mm × 10 mm x 0.2mm 99.9% metals basis gold ablation target was prepared from a sputtering target (Agar Scientific, UK). This target piece was then affixed to a stage, fabricated using PlasClear photopolymer resin and a Freeform Pico (Asiga, CA, USA) 3D printer. The depositions were performed using a 1064 nm diode-pumped, solid state neodymium-doped yttrium aluminium garnet (Nd:YAG) laser. This laser was operated in TEM_{00} mode, producing a beam with a Gaussian profile and a spot diameter of 140µm at the focus. This beam was pulsed at a rate of 10kHz, with a pulse width of 700ps. The pulsed laser beam was rastered across the target during sample production using a 2D scanning galvanometer (Raylase SS-12, Germany). The position of the target in the beam waist was controlled using an M-404 4PD nanoposition stage (PI, Germany). Design of Experiments (DoE) and data analysis was performed with the aid of StatEase Design Expert 7 and Origin Pro 2016 software packages respectively. Parameters to be examined in the DoE were selected based on the criteria that they should be factors controlled by the laser setup and as a result these parameters were the laser fluence, the laser scan speed and the raster scan spacing.

2.2 Experimental Setup and Method

The deposition of films for this optimisation study was carried out via the CAP technique, utilising the laser and galvanometer to raster scan a 1064 nm, 10 kHz incident laser beam across the across the surface of the gold foil target through a COP substrate (Figure 1).

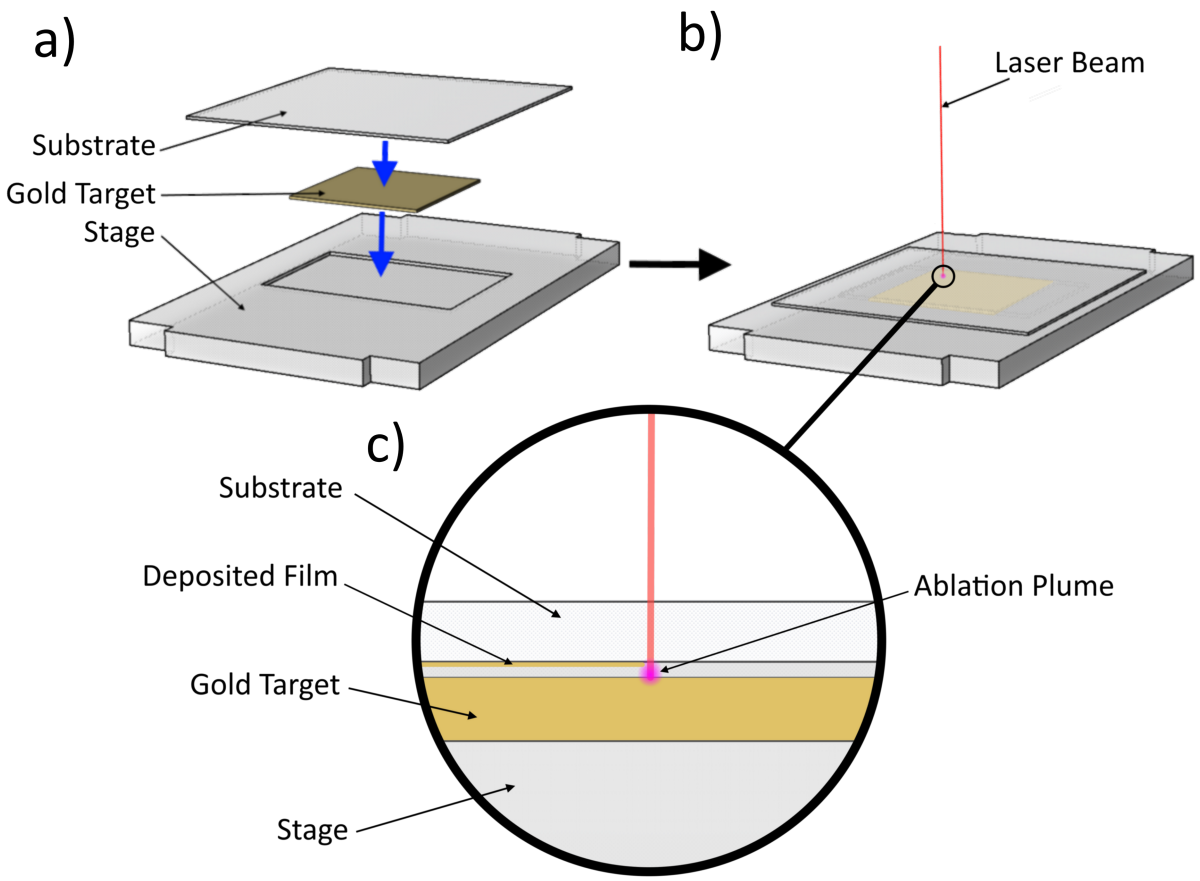

Fig. 1. Schematic of a CAP experimental setup representing the deposition of a gold nanostructured film onto a substrate.

During ablation, the target was adhesively affixed to the stage inside and indentation with a depth 50 µm greater than that of the target, producing a 50 µm gap between the target and the substrate. The beam was unidirectionally rastered across the target (travelling unidirectionally for each individual scanline) in a 5 x 5 mm square pattern. Thus, once the raster scan pattern was completed a single time a 5mm x 5mm square area of nanostructured gold thin-film had been deposited that was suitable for characterisation. Parameters for the production of the samples were selected using Design Expert to select values within known ranges at which CAP occurs. These parameters were selected to create a 2-level factorial, 3 factor integration DOE and the resulting sample set was produced in duplicate to reduce error. Numerous samples were prepared using this method to examine the effects of fluence (from 0.221 J/cm^2 to 0.481 J.cm^2), scan spacing (that is, the gap between each raster scanned line, varied from 50 µm to 150 µm) and scan speed (from 6 mm/s to 18 mm/s) on the films deposited.

2.3 Film Characterisation

The resulting samples were characterised via UV-Vis spectroscopy (Agilent, Cary 50, USA). Samples were carbon coated using a Scancoat Six (Edwards, UK) with carbon evaporation accessory at a pressure of 10^{-4} bar for examination via Scanning Electron Microscopy (SEM) using an Evo LS15 (Carl Zeiss AG). Image analysis on the SEM images obtained was carried out using Fiji image analysis software [31]. The resulting data was input into the DoE to develop a mathematical model that would allow for control over the process.

3. Results and Discussion

The test samples were successfully prepared in atmospheric conditions, at room temperature using only the gold target, 2D motorized stage, COP substrate and 1064nm laser. Such a practical example of this simple, direct methodology working as described suggests that this technique is an environmentally friendly alternative to many existing techniques. In addition, the depositions were performed with ablation times ranging from 9 seconds (scan speed: 18 mm/s, scan spacing: 150 µm) to 83 seconds (scan speed: 6mm/s, scan spacing: 150 µm) for the deposition of a square with an area of 25 mm^2. The exact deposition parameters and sample numbers used during this investigation are listed in Table 1.

Table 1. A list of the deposition parameters for samples produced. Multiple samples were produced for each combination of parameters.

Sample numbers	Fluence (J/cm^2)	Scan Speed (mm/s)	Scan Spacing (µm)
1, 14	0.221	6	50
2, 15	0.221	18	50
3, 16	0.481	6	50
4, 17	0.481	18	50
5, 18	0.221	6	150
6, 19	0.221	18	150
7, 20	0.481	6	150
8, 21	0.481	18	150
9, 10, 11, 12, 13, 22, 23, 24, 25, 26	0.351	12	100

The samples resulting from these depositions appeared as squares on the COP substrate, ranging in colour from red to brown. The deposited films appeared matte when in a face-up

orientation, and appeared shiny when viewed from the opposite side due to the shininess of the COP substrate. These samples were then characterised using Scanning Electron Microscopy (SEM) and UV/Vis spectroscopic analysis of their plasmonic properties. The resulting characterisation data was then analysed to find any statistically significant relationships between the process parameters and the properties of the films produced.

3.1 Film Morphology

SEM analysis showed the formation of nanostructures for all parameters tested. These structures shared a similar morphology, being comprised of smaller, fused or aggregated nanoparticles. Upon further examination, a degree of variation was noted in the size of these structures and the homogeneity of their deposition at differing ablation parameters (Figure 2).

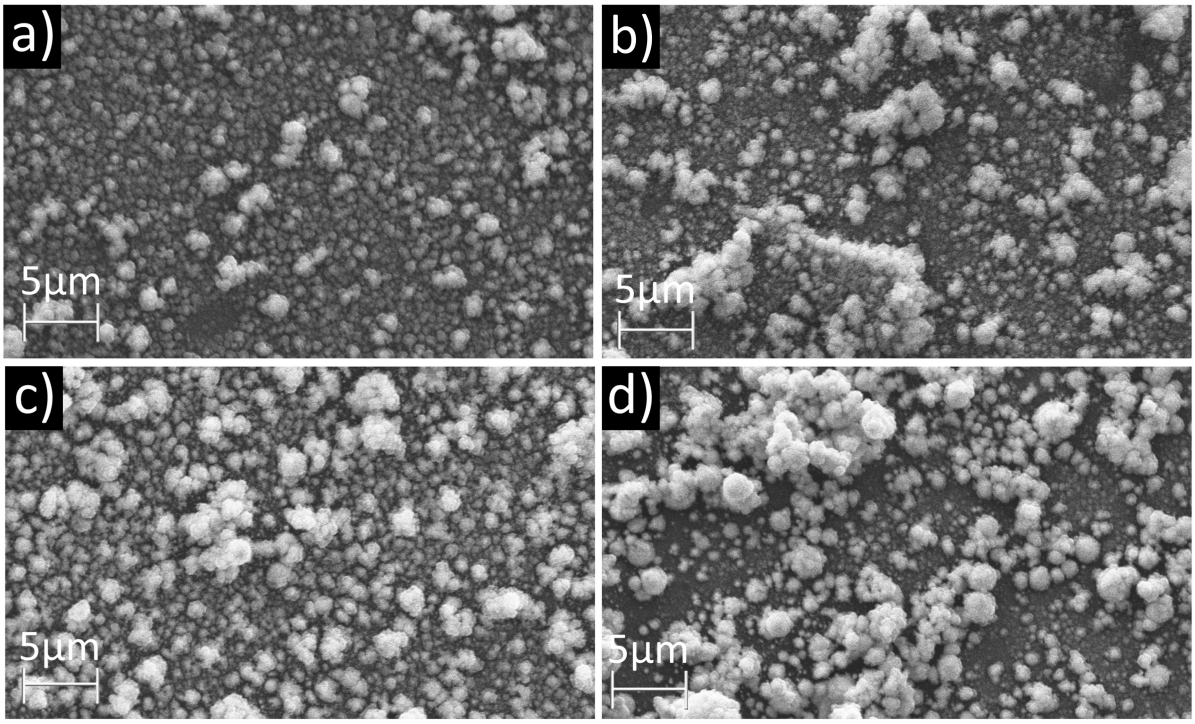

Fig. 2. SEM images of samples a): 18 (6 mm/s, 0.221 J/cm^2, 150 µm), b): 11 (12 mm/s, 0.351 J/cm^2, 100 µm), c): 20 (12 mm/s, 0.481 J/cm^2, 150 µm) and d): 4 (18 mm/s, 0.481 J/cm^2, 50 µm) at 8380× magnification.

While similar structures to those shown in Figure 2 were present in every sample, the specific images shown were chosen because they exhibit some of the clearest examples of the structures discussed herein. Figure 2a is an example of one of the more homogenous films obtained at lowest fluence, lowest scan speed and highest scan spacing (6 mm/s, 0.221 J/cm^2,

150 µm), clearly showing less large scale aggregation and fewer large spheroidal structures than other films presented. In contrast, Figures 2b and 2c show less homogenous films, with 2b showing evidence of large aggregated structures forming and 2c showing even more aggregate formation than b. Figure 2d shows an example of a film comprised of a mix of nanoparticles, micro-scale nanoparticle aggregates and larger spheroidal microparticles. It is hypothesised that the larger spheroidal microparticle structures observed (Figure 2d) may be the result of the laser melting and sintering deposited micro-scale nanoparticle aggregates into the spheroidally lobed structures present [32]. These aggregated structures with a broccoli-like appearance would suggest that the deposited film has a high ratio of surface area to volume, a property that is extremely desirable for their proposed application in biosensors [33].

All parameter sets within the window tested resulted in a densely packed nanostructured film. As mentioned previously some parameters (e.g. sample 18, Figure 2a) resulted in relatively uniform films while other parameters (e.g. sample 4, Figure 2d) resulted in aggregated clusters of varying size.

Following this, the SEM images obtained were analysed by manual particle sizing. During particle sizing fifty particles from each sample were chosen using a script that randomly placed points on the image. The particles marked by these points were then sized by manual ellipse fitting to obtain a major axis, minor axis, area and eccentricity measurement for each. Average responses were calculated for each sample based on the fifty random particles measured in their respective SEM images (Table 2). Standard deviations were also recorded as a measurement of the dispersity of the particles produced.

Table 2. Particle size analysis results (with standard deviation indicated, n=50).

Sample	Avg Minor Axis (nm)	Avg Major Axis (nm)	Avg Area (nm^2)	Avg Eccentricity
1	223 ± 56	277 ± 80	206656 ± 114236	0.51 ± 0.24
2	147 ± 38	178 ± 51	87605 ± 49284	0.46 ± 0.27
3	207 ± 52	237 ± 62	162682 ± 86446	0.36 ± 0.29
4	235 ± 60	279 ± 72	217593 ± 109501	0.44 ± 0.26
5	218 ± 54	259 ± 74	188430 ± 99363	0.45 ± 0.25
6	213 ± 49	256 ± 58	178859 ± 88137	0.48 ± 0.25
7	190 ± 51	211 ± 56	134316 ± 77813	0.31 ± 0.28

8	235 ± 89	267 ± 101	223402 ± 210179	0.35 ± 0.28
9	265 ± 89	326 ± 113	300751 ± 205286	0.52 ± 0.20
10	246 ± 76	292 ± 90	243338 ± 143070	0.40 ± 0.30
11	325 ± 130	393 ± 153	458533 ± 429958	0.50 ± 0.23
12	250 ± 77	290 ± 80	244364 ± 135750	0.40 ± 0.29
13	232 ± 74	269 ± 81	212695 ± 126095	0.40 ± 0.29
14	275 ± 111	315 ± 130	314306 ± 251533	0.36 ± 0.28
15	279 ± 89	317 ± 100	303490 ± 185652	0.37 ± 0.27
16	255 ± 97	302 ± 118	275351 ± 241689	0.44 ± 0.26
17	237 ± 114	279 ± 124	249940 ± 248796	0.46 ± 0.25
18	212 ± 56	252 ± 72	178973 ± 104235	0.42 ± 0.29
19	179 ± 50	214 ± 61	128846 ± 71535	0.44 ± 0.27
20	203 ± 38	239 ± 50	157441 ± 61204	0.41 ± 0.28
21	229 ± 77	270 ± 91	214174 ± 141208	0.44 ± 0.27
22	201 ± 46	235 ± 52	154822 ± 67590	0.41 ± 0.28
23	317 ± 88	375 ± 102	398039 ± 231149	0.49 ± 0.19
24	227 ± 57	262 ± 63	196858 ± 103835	0.37 ± 0.29
25	194 ± 44	226 ± 53	143565 ± 67644	0.41 ± 0.28
26	230 ± 69	287 ± 89	223061 ± 131796	0.51 ± 0.25

3.2 Optical Properties

The deposited films were also examined using UV-Vis spectroscopy. These spectra were obtained to examine the plasmonic properties of the films and to allow for an examination of the effect of various ablation parameters on those resulting plasmonic properties. Following analysis, the UV-Vis spectra obtained from these samples were then subjected to baseline correction (to remove the broad background peak due to the ablated COP) and peak analysis. This analysis was used to find the local maxima (suggested to be largely indicative of particle size [34]) and the area under the peak (i.e. its intensity, suggested to be indicative of the relative thickness of the film deposited [35]). The spectra obtained showed broad plasmonic peaks in the 530 nm to 580 nm range, with a distinctive shape that tapers off more gradually on the longer wavelength side of the peak than it does on the shorter wavelength side. This skewing is evident in the minima observed for the peaks obtained. The shorter wavelength minima of the peaks (on the left side of the spectrum as graphed) observed were at approximately 450 nm, which is 105 nm from the median of the range in which the maxima were found (555 nm). Meanwhile the longer wavelength minima (on the right side of the

spectrum as graphed) were generally at approximately 800nm, which is 245 nm from the median of the range for the maxima. Figure 3 shows an example of a typical UV-Vis spectrum obtained, as well as baseline corrected peaks for several samples exhibiting the variations observed in peak position and intensity.

Table 3. The results of peak analysis performed on the UV-Vis spectrum of each individual sample.

Sample no.	Plasmonic Peak Wavelength (nm)	Plasmonic Peak Integral	Plasmon Peak Full Width at Half Maximum (nm)
1	561	28.1	160
2	568	26.3	151
3	570	47.7	146
4	576	40.9	170
5	551	11.1	147
6	550	12.3	138
7	572	35.6	163
8	574	26.1	152
9	568	21.8	161
10	571	23.3	164
11	568	22.3	164
12	577	49.9	225
13	576	30.4	193
14	562	33.1	161
15	559	15.6	151
16	564	38.9	146
17	579	45.1	163
18	559	18.5	154
19	557	21.2	150
20	578	42.7	169
21	566	34.5	134
22	568	29.8	155
23	568	33.5	142

24	570	32.5	151
25	568	25.0	146
26	572	28.8	164

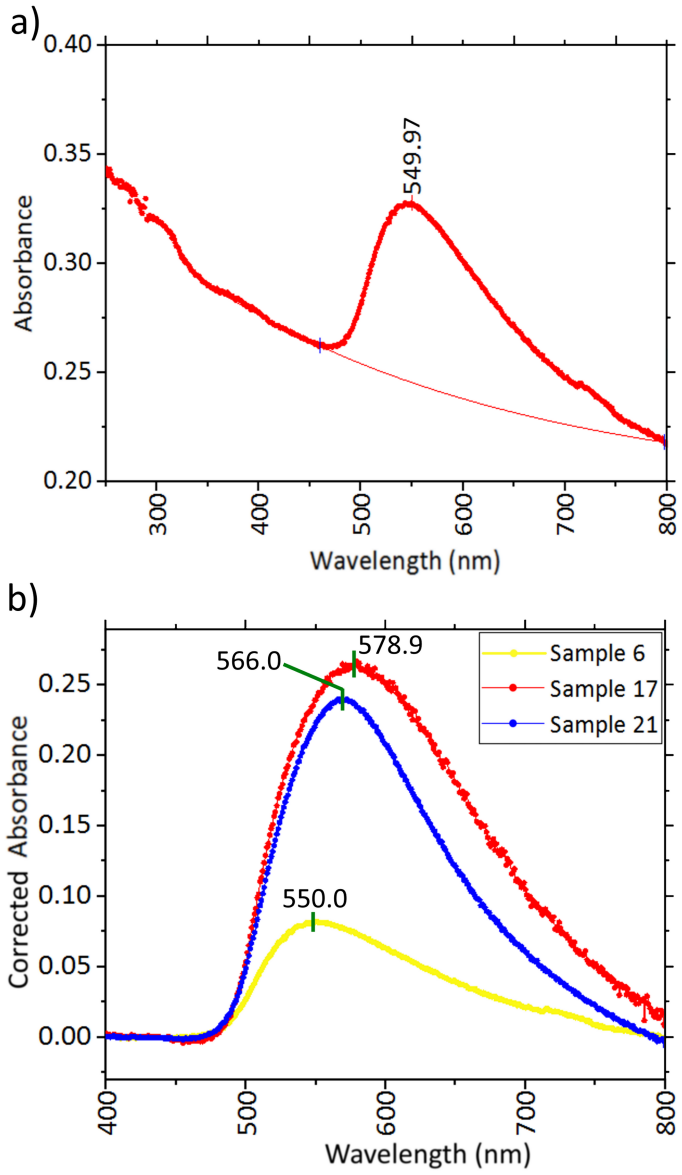

Fig. 3. Typical UV-Vis spectra of the samples obtained after CAP deposition of gold nanostructures onto COP. a) The UV-Vis spectrum of sample 6 showing the corrected baseline and the plasmonic peak at around 550 nm; and b) UV-Vis spectra of samples 6, 17 and 21 exhibiting varying intensities of peaks ranging from 550 nm to 578 nm obtained at different CAP parameters.

The broad background feature in the UV-Vis spectra obtained are likely a result of the effects of the laser on the COP substrate. Based on previous investigations, the effects of a direct incident laser beam focussed on COP at the selected fluences are understood to result in a small degree of polymer oxidation (in the form of carbonylation) and the ablation of channels with a depth of up to approximately 40µm and a width of up to approximately 120µm [36]. Additionally, studies involving the deliberate oxidation of various similar COP samples resulted in the formation of carbonyl groups and comparable features in the UV-Vis spectra observed [37]. Based on this it is reasonable to expect that the effects of such a laser on COP placed 50µm above the focal point would be similar and that the resulting oxidation is the source of the broad baseline peak.

3.3 Signal-to-Noise Ratio Analysis

During analysis, a signal-to-noise (SNR) value was calculated for each experimental output recorded. This SNR value was calculated to determine the contribution of random noise in each output dataset. As such, these SNR values provide a means for assessing how accurately the instruments and methodologies used during characterisation were able to measure the response values. Because the data obtained falls within the scope of image processing and analytical chemistry (specifically, spectroscopic analysis) it was decided that the SNRs should be calculated using the formulae considered standard in these fields. In image processing (with the exception of direct electronic signal analysis) SNR is most often calculated using minor variations on the true SNR formula [38,39] (that is the mean signal (μ) over the standard deviation of the dataset (σ) [40]). The “true SNR” formula is also commonly used in analytical chemistry [40]. As such, it was decided the SNR of the collected data should also be calculated using the true SNR formula. The resulting SNRs were then converted to decibels by the application of a logarithmic operation. As such, all SNR values for each dataset were calculated according to the following formula:

$SNR = 10(\log_{10}(\mu/\sigma))$

The signal to noise ratio was calculated for each response measured during the course of this study and the results can be seen in Table 4.

Table 4. The calculated mean signal, standard deviation and signal-to-noise ratio of each response dataset collected.

	Mean Signal	Standard Deviation	Signal-to-Noise Ratio (dB)
Plasmonic Peak Position (nm)	567.403	7.780	18.629
Plasmonic Peak Integral	29.802	10.379	4.581
Plasmonic Peak FWHM (nm)	158.542	18.137	9.416
Average Minor Axis (nm)	231.732	39.342	7.701
Minor Axis Standard Deviation (nm)	70.416	24.714	4.547
Average Major Axis (nm)	273.232	47.588	7.590
Major Axis Standard Deviation (nm)	83.740	27.564	4.826
Average Area (nm^2)	223003.431	82828.358	4.301
Area Standard Deviation (nm^2)	145499.342	85472.142	2.310
Average Eccentricity	0.427	0.0553	8.879
Eccentricity Standard Deviation	0.265	0.0266	9.978

The SNR analysis results show that the plasmonic peak position output gave the strongest response relative to noise suggesting that this value was the one most accurately quantified by

the instruments and characterisation methods used. Conversely, the area standard deviation response gave the lowest response relative to noise.

3.4 Analysis of Variance (ANOVA)

With the aid of Design Expert 7 DOE software, each of the output datasets were examined to derive models relating the processing parameters to the resulting responses. From the responses recorded four statistically significant model equations were derived describing the effects influencing the observed area of the deposited particles (representative of their size), the standard deviation of those area measurements (representative of the particle dispersity), the plasmonic peak position, plasmonic peak integral. The full results of the ANOVA analyses for these models can be seen in Table 5.

Table 5. The ANOVA ouptuts for each of the models derived. More detailed tables are available in Supplementary Figures 1-4.

Response	Degrees of Freedom	Adjusted R^2	Predicted R^2	Adequate Precision	F Value
Particle Area	7	0.4952	0.2850	8.682	4.50
Area Standard Deviation	7	0.4985	0.3312	8.021	4.55
Plasmonic Peak Position	5	0.5922	0.4085	9.528	8.26
Plasmonic Peak Integral	2	0.5990	0.5380	12.440	19.67

The ANOVA results for each of these derived models found that both size models have an adjusted R^2 of approximately 0.5, while each plasmonic peak based model has an adjusted R^2 of greater than 0.59. All models were found to have an adequate precision of greater than 8, which is well in excess of the desired value of at least 4 for a statistically significant model [41]. The F-value for the model describing the plasmonic peak integral is large (19.67). The F-value of the plasmonic peak position model (8.26) is smaller but still significant. Both particle size related models have an F value of ~4.5, which are also statistically significant values.

The ANOVA tables presented provide a great deal of information about the models derived when considered within the context of the SNR values of the outputs examined. The relatively high SNR of the plasmonic peak position data (18.63 dB) suggests that this model is significant but has a high degree of variance. Considering this fact, and that the F-value of the peak position model is lower than would be expected for such a correlated, high SNR, high adequate precision model it seems likely that the inclusion of an independent variable for scan speed in the model is increasing the observed variance. This is, however, unavoidable within the context of the DoE tools being used as the Design Expert 7 software package does not allow for the derivation of non-hierarchical models and the scan speed has a statistically significant interaction with the scan spacing. Conversely, the lower but still acceptable SNR for the plasmonic peak integral (4.581) with a higher F-value suggests that the observed variance in the data is primarily a result of noise. Similarly, the SNR values of the area and standard deviation of area models (4.301 and 2.310 respectively) suggest much of the observed variance in these models is due to noise, while the lower F value suggests that these models are the least statistically significant of all the models obtained. The higher levels of noise observed in some datasets could be reduced by further expanding the process space being examined or could be indicating that a highly significant process affecting this property is not being controlled.

3.5 Particle Morphology Models

With the aid of ANOVA analysis performed by DoE software, two statistically significant mathematical models were found describing features related to the morphology of the particles deposited (Figure 4). The first relationship found describes an inverse squared relationship between the area of the deposited particles (A) and all processing parameters measured. In this case the area serves as a measurement of the size of the particles, as the area of the particles on an SEM image should be proportional to their size. The derived equation is as follows:

$$A = (-1.32e^{-4}\nu - 5.18e^{-3}F - 1.52e^{-5}d + 4.15e^{-4}\nu F - 1.95e^{-6}\nu d + 6.04e^{-5}Fd + 5.62e^{-6}\nu Fd + 3.30e^{-3})^{-2}$$

This equation suggests that the strongest contribution to the size of the particles is made by the fluence parameter (F). This model equation also suggests that there are many interactions

between the selected processing parameters that also influence the particle size, including a complex 3-way interaction between fluence, scan speed (v) and scan spacing (d), as shown by the presence of the vFd component of the equation.

This analysis also yielded an equation describing the influence of the processing parameters on the standard deviations of the areas of the deposited particles (σ_A). Given that the area of the particles serves as a measurement of their size, the standard deviation of the areas should thus serve as a suitable measurement of the dispersity of the deposited particles (i.e. the homogeneity of the film). As such, an inverse cubed relationship between the processing parameters and the dispersity of the particles was found according to the following equation:

$$\sigma_A = (-7.23e^{-4}v - 0.044F - 1.15e^{-4}d + 2.39e^{-3}vF + 1.21e^{-5}vd + 5.11e^{-4}Fd - 3.69e^{-5}vFd + 0.029)^{-3}$$

Similar to the equation describing the area of the particles, this equation suggests that the dispersity is primarily influenced by the fluence of the incident laser and that there are many interactions present.

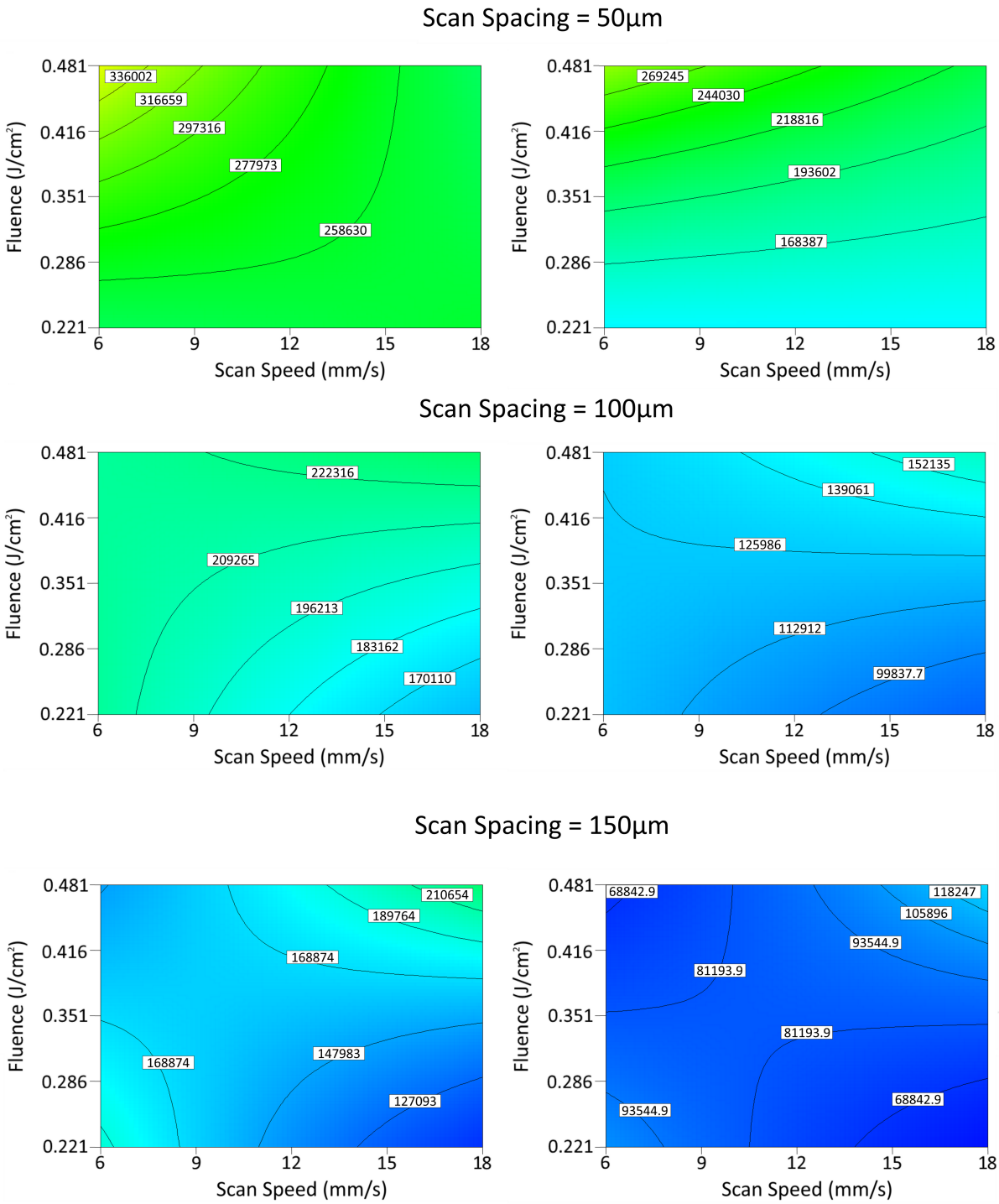

348

349 **Fig. 4.** Contour plots of the areas (left) and the standard deviations of areas (right) predicted
350 by the derived models based at various scan spacings (50µm, 100µm and 150µm)

351 The agreement of this model with the practical results was evaluated with the aid of a normal
352 plot of its residuals and a plot of predicted vs actual values (Figure 5). It can be seen from

these graphs that deviations from the model are approximately normal and there are no obviously significant outliers in either dataset.

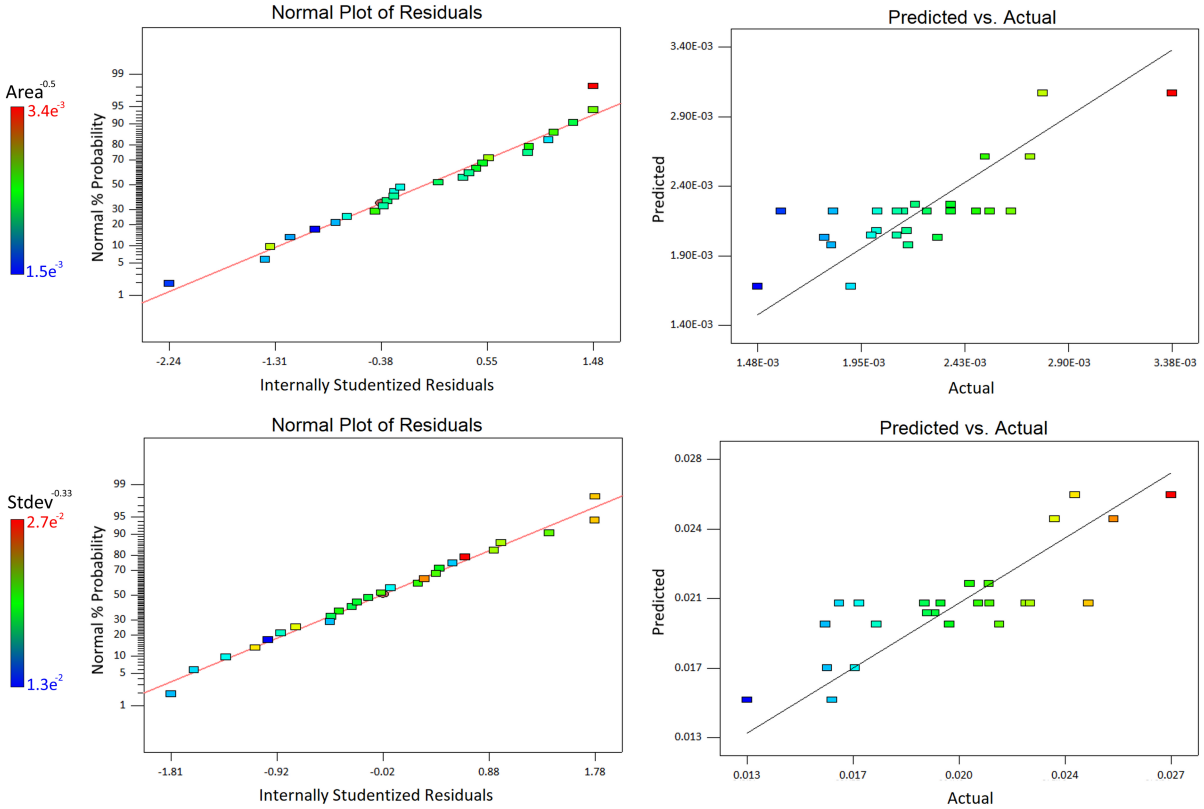

Fig. 5. The normal plot of residuals and predicted vs actual plot for the size model derived (top) and the dispersity model derived (bottom).

3.6 Plasmonic Peak Position Model

Similar to the analysis in Section 3.5, a statistically significant model was found describing a relationship between the deposition parameters and the plasmonic peak position (λ_p) of the resulting film. This model is summarised by the following equation:

$$\lambda_p = 0.91v + 21.1F - 0.06d - 0.008vd + 0.003Fd + 553.05$$

Of the deposition parameters tested, this model denotes the scan speed (v), fluence (F) and scan spacing (d) as the primary determining factors in the observed plasmonic peak position. Based on this equation it is evident that the primary factor influencing the plasmonic peak position is the fluence imparted during ablation, with higher fluences resulting in films with longer plasmonic wavelengths (Figure 6). In nanostructured materials, longer plasmonic

wavelengths are generally known to be a result of larger particle size [34]. As such, this trend suggests that higher fluences may result in either the deposition of larger particles or more melting of the deposited structures, causing them to behave as if they were larger particles. This observation agrees with the formulae presented in Section 3.5, which also suggest that a higher fluence results in larger particle size. This model also suggests that there are statistically significant scan speed/scan spacing interactions and fluence/scan spacing interactions present in the data, as shown by the presence of the vd and Fd components of the equation.

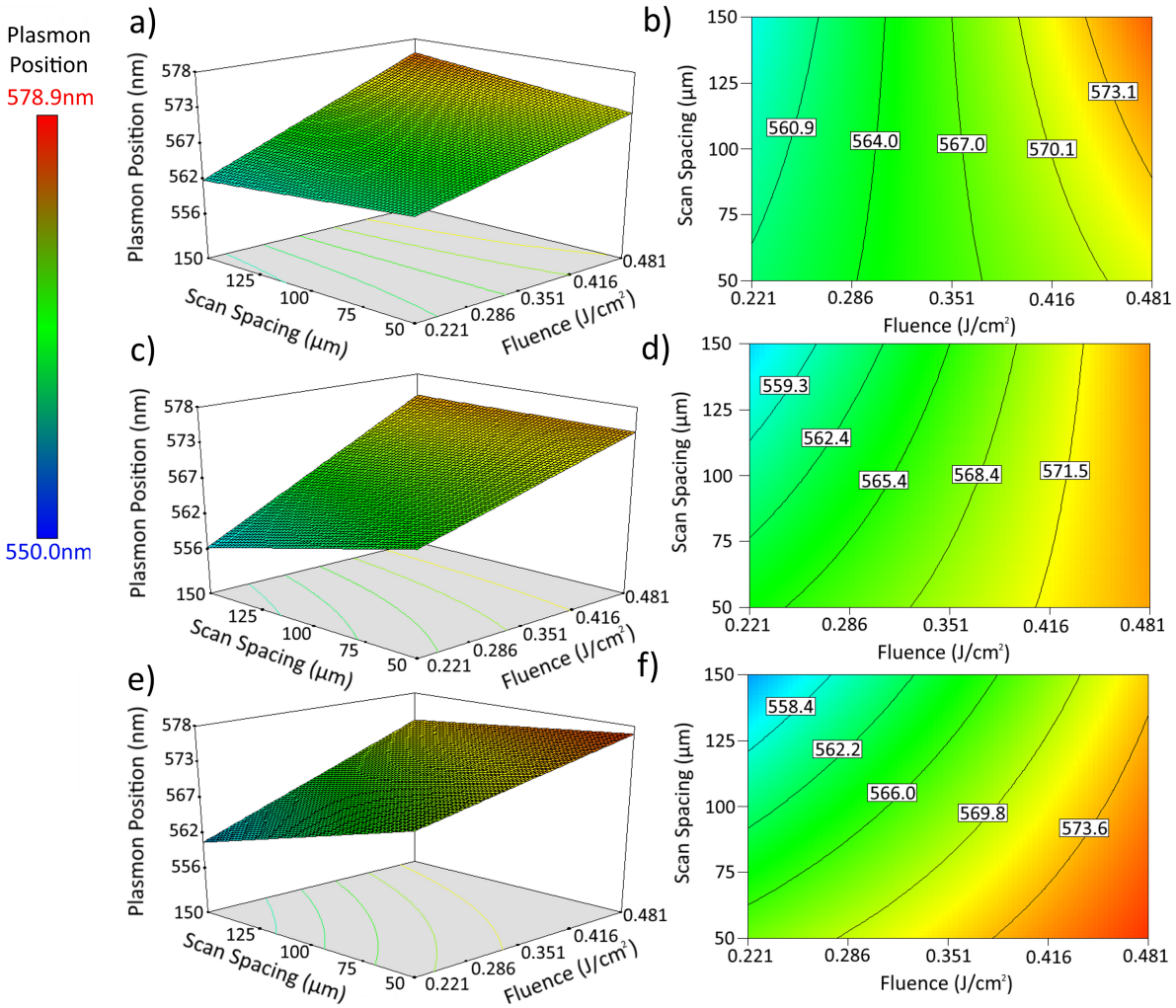

Fig. 6. Surface plots and contour plots of the plasmonic peak positions predicted by the derived model at scan speeds of 6mm/s (a,b), 12mm/s (c,d) and 18mm/s (e,f).

By reviewing the normal plot of residuals and predicted vs actual graphs produced by this model (Figure 7) it can be seen that the derived equation agrees with the experimental data obtained, showing no significant outliers in the dataset.

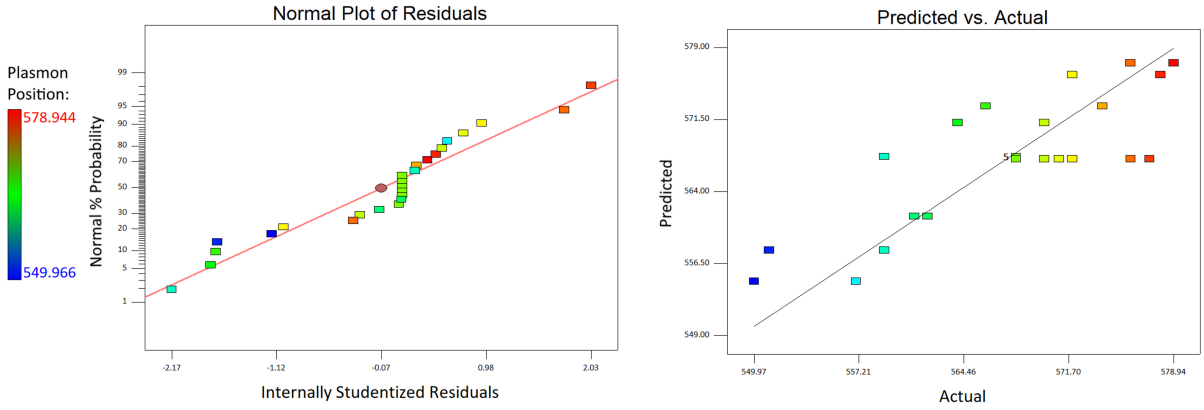

Fig. 7. The normal plot of residuals and predicted vs actual plot for the plasmonic peak position model derived.

3.7 Plasmonic Peak Area Model

A statistically significant model was also found describing the area under the plasmonic peak (A) found using integration of each sample in terms of the fluence (F) and scan spacing (d) used during deposition (Figure 8). This relationship can be summarised in the following equation:

$$A = 44.36F^2 + 0.000081d^2 + 52.34F - 0.070d - 0.12Fd + 15.44$$

This model proposes that there is a squared relationship between the significant processing parameters and the area under the plasmonic peak. This model also suggests that there are statistically significant interactions between the fluence and scan spacing present, as can be seen by the presence of an Fd component in the model equation.

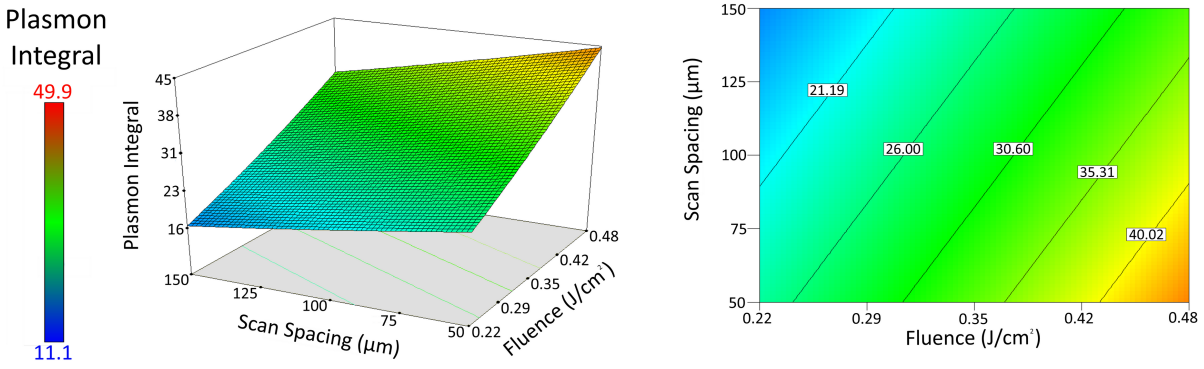

Fig. 8. A surface plot and contour plot of the predicted integral (i.e. the predicted area) of the plasmon peaks in terms of the scan spacing and fluence at which samples are produced.

As with the models presented in sections 3.5 and 3.6, a normal plot of residuals and predicted vs actual plot (Figure 9) comparing the data obtained with the predictions of this model were used to evaluate its agreement with observed reality. The normal plot of residuals for this model shows that deviations of observed data from predicted values are mostly normal, with a single apparent outlier (sample number 12) visible in the upper right area of the graph. Similarly, the predicted vs actual graph shows reasonable agreement, with a single apparent outlier on the right-hand side of the graph that is also sample number 12. Sample number 12 was only one of 10 repetitions of the specific set of processing parameters used in its production and the other 9 are in agreement with each other. As such, it seems safe to conclude that sample number 12 is simply a statistical outlier in the plasmonic peak integral dataset.

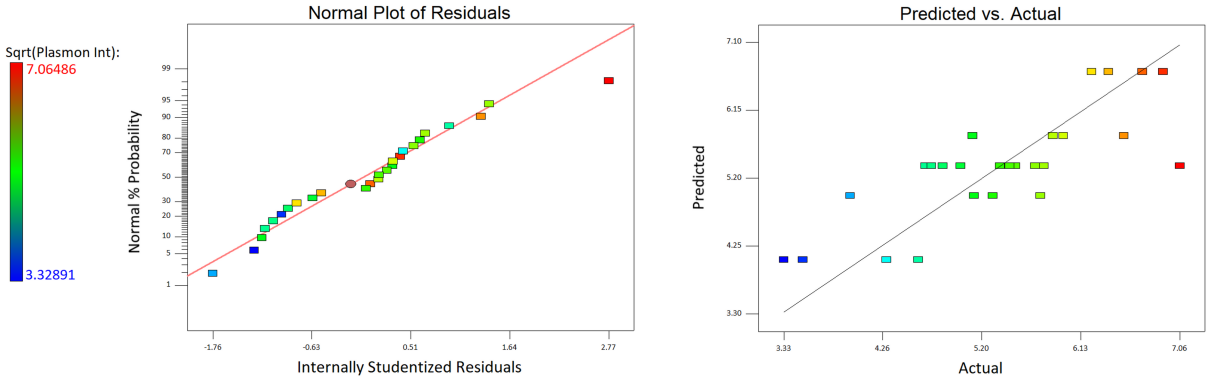

Fig. 9. The normal plot of residuals and predicted vs actual plot for the plasmonic peak integral model derived.

4. Conclusions

The use of CAP for rapid, single-step, green deposition of gold nanostructures has been demonstrated. This process results in the deposition of nanostructures with potential applications in sensor development (through functionalization of the nanostructures with DNA) and catalysis due to their high surface area morphology, as observed by SEM. Studies on the resulting surfaces have yielded statistically significant mathematical models describing relationships between the processing parameters and some of the properties of the resulting films.

SEM imaging of the samples showed a range of structure morphologies and dense packing at all parameters tested. Mathematical models derived suggest that the size and dispersity of the

particles deposited (as determined by SEM area measurements and the standard deviation of those measurements) are primarily determined by fluence and a large number of interactions between all processing parameters tested. While these models were statistically significant, their significance was not extremely high, suggesting that the parameters tested may not be the primary determiners of particle morphology. It is possible that parameters not investigated (such as ambient temperature and pressure, ambient gas, sample-substrate distance, laser wavelength, pulse repetition frequency and pulse width) may allow for greater control over particle size and film homogeneity than the parameters tested. Future work will likely examine this possibility in more depth. Future process examination via optical emission spectroscopy will also help to confirm or refute a hypothesised link between the mechanisms of CAP and PLD. Optical emission spectroscopy will also help to elucidate the specific details of the plume dynamics during CAP which will further facilitate the development and optimisation of this technique.

The derived models also suggest that the wavelength of the local maximum for the plasmonic peak is primarily determined by the fluence and the scan speed, with a minor effect being had by scan-spacing and interactions that are present between the significant parameters. Finally, it was found that the area under this peak is influenced by the fluence and the scan spacing used during sample production with interactions between these parameters also having an influence.

Acknowledgements

This publication has emanated from research conducted with the financial support of the European Union's Horizon 2020 Research and Innovation programme under the Marie Sklodowska-Curie grant agreement No. 655194 and Science Foundation Ireland (SFI) under Grant Number 12/IA/1576.

References

[1] Mohammed AM. Fabrication and characterization of gold nano particles for DNA biosensor applications. Chinese Chem Lett 2016;27:801–6. doi:10.1016/j.cclet.2016.01.013.

[2] Peng H, Tang H, Jiang J. Recent progress in gold nanoparticle-based biosensing and cellular imaging. Sci China Chem 2016;59:783–93. doi:10.1007/s11426-016-5570-7.

[3] Zeng S, Yong K-T, Roy I, Dinh X-Q, Yu X, Luan F. A Review on Functionalized Gold Nanoparticles for Biosensing Applications. Plasmonics 2011;6:491–506. doi:10.1007/s11468-011-9228-1.

[4] Anker JN, Hall WP, Lyandres O, Shah NC, Zhao J, Van Duyne RP. Biosensing with plasmonic nanosensors. Nat Mater 2008;7:442–53. doi:10.1038/nmat2162.

[5] Daggumati P, Matharu Z, Seker E. Effect of Nanoporous Gold Thin Film Morphology on Electrochemical DNA Sensing. Anal Chem 2015;87:8149–56. doi:10.1021/acs.analchem.5b00846.

[6] Bouvrée A, D'Orlando A, Makiabadi T, Martin S, Louarn G, Mevellec JY, et al. Nanostructured and nanopatterned gold surfaces: application to the surface-enhanced Raman spectroscopy. Gold Bull 2013;46:283–90. doi:10.1007/s13404-013-0127-4.

[7] Wen Z-Q, Li G, Ren D. Detection of Trace Melamine in Raw Materials Used for Protein Pharmaceutical Manufacturing Using Surface-Enhanced Raman Spectroscopy (SERS) with Gold Nanoparticles. Appl Spectrosc Vol 65, Issue 5, Pp 514-521 2011;65:514–21. doi:10.1366/10-06089.

[8] Takale BS, Bao M, Yamamoto Y. Gold nanoparticle (AuNPs) and gold nanopore (AuNPore) catalysts in organic synthesis. Org Biomol Chem 2014;12:2005. doi:10.1039/c3ob42207k.

[9] Gutiérrez L-F, Hamoudi S, Belkacemi K. Synthesis of Gold Catalysts Supported on Mesoporous Silica Materials: Recent Developments. Catalysts 2011;1:97–154. doi:10.3390/catal1010097.

[10] Zhao P, Li N, Astruc D. State of the art in gold nanoparticle synthesis. Coord Chem Rev 2013;257:638–65. doi:10.1016/j.ccr.2012.09.002.

[11] Choy KL. Chemical vapour deposition of coatings. Prog Mater Sci 2003;48:57–170. doi:10.1016/S0079-6425(01)00009-3.

[12] George SM. Atomic Layer Deposition: An Overview. Chem Rev 2010;110:111–31. doi:10.1021/cr900056b.

[13] Emslie DJH, Chadha P, Price JS. Metal ALD and pulsed CVD: Fundamental reactions

and links with solution chemistry. Coord Chem Rev 2013;257:3282–96. doi:10.1016/j.ccr.2013.07.010.

[14] Stratakis E, Ranella A, Farsari M, Fotakis C. Laser-based micro/nanoengineering for biological applications. Prog Quantum Electron 2009;33:127–63. doi:10.1016/j.pquantelec.2009.06.001.

[15] Kumar R, Kumar G, Umar A. Pulsed Laser Deposited Nanostructured ZnO Thin Films; A Review. J Nanosci Nanotechnol 2014;14:1911–30. doi:10.1166/jnn.2014.9120.

[16] Piqué A, Kim H, Auyeung RCY, Beniam I, Breckenfeld E. Laser-induced forward transfer (LIFT) of congruent voxels. Appl Surf Sci 2016;374:42–8. doi:10.1016/j.apsusc.2015.09.005.

[17] Dhami G, Tan B, Venketakrishnan K. Laser induced reverse transfer of gold thin film using femtosecond laser. Opt Lasers Eng 2011;49:866–9. doi:10.1016/j.optlaseng.2011.02.019.

[18] Adrian FJ, Bohandy J, Kim BF, Jette AN, Thompson P. A study of the mechanism of metal deposition by the laser-induced forward transfer process. J Vac Sci Technol B 1987;5:1490–4. doi:10.1116/1.583661.

[19] Henley SJ, Carey JD, Silva SRP. Pulsed-laser-induced nanoscale island formation in thin metal-on-oxide films. Phys Rev B - Condens Matter Mater Phys 2005;72:1–10. doi:10.1103/PhysRevB.72.195408.

[20] Trice J, Thomas D, Favazza C, Sureshkumar R, Kalyanaraman R. Pulsed-laser-induced dewetting in nanoscopic metal films: Theory and experiments. Phys Rev B - Condens Matter Mater Phys 2007;75:1–15. doi:10.1103/PhysRevB.75.235439.

[21] Ruffino F, Pugliara A, Carria E, Romano L, Bongiorno C, Spinella C, et al. Novel approach to the fabrication of Au/silica coreshell nanostructures based on nanosecond laser irradiation of thin Au films on Si. Nanotechnology 2012;23. doi:10.1088/0957-4484/23/4/045601.

[22] Lu L-X, Wang Y-M, Srinivasan BM, Asbahi M, Yang JKW, Zhang Y-W. Nanostructure Formation by controlled dewetting on patterned substrates: A combined

theoretical, modeling and experimental study. Sci Rep 2016;6:32398. doi:10.1038/srep32398.

[23] Pandey P, Kunwar S, Sui M, Bastola S, Lee J. Role of annealing temperature, time, and composition on the fabrication of AUxPd1-xnanostructures on c-plane sapphire by the solid-state dewetting of bimetallic thin films. IEEE Trans Nanotechnol 2018;17:325–31. doi:10.1109/TNANO.2018.2801943.

[24] McCann R, Hughes C, Bagga K, Stalcup A, Vázquez M, Brabazon D. Pulsed laser deposition of plasmonic nanostructured gold on flexible transparent polymers at atmospheric pressure. J Phys D Appl Phys 2017;50:245303.

[25] Kwok H., Kim H., Kim D., Shen W., Sun X., Xiao R. Correlation between plasma dynamics and thin film properties in pulsed laser deposition. Appl Surf Sci 1997;109–110:595–600. doi:10.1016/S0169-4332(96)00640-X.

[26] Donnelly T, Lunney JG. Confined laser ablation for single-shot nanoparticle deposition of silver. Appl Surf Sci 2013;282:133–7. doi:10.1016/j.apsusc.2013.05.083.

[27] Nikov RG, Dikovska AO, Nedyalkov NN, Avdeev G V., Atanasov PA. Au nanostructure fabrication by pulsed laser deposition in open air: Influence of the deposition geometry. Beilstein J Nanotechnol 2017;8:2438–45. doi:10.3762/bjnano.8.242.

[28] Rajendiran S, Rossall AK, Gibson A, Wagenaars E. Modelling of laser ablation and reactive oxygen plasmas for pulsed laser deposition of zinc oxide. Surf Coatings Technol 2014;260:417–23. doi:10.1016/j.surfcoat.2014.06.062.

[29] Jimenez A, Lepage D, Beauvais J, Dubowski JJ. Study of surface morphology and refractive index of dielectric and metallic films used for the fabrication of monolithically integrated surface plasmon resonance biosensing devices. Microelectron Eng 2012;93:91–4. doi:10.1016/j.mee.2011.10.016.

[30] Sharma R, Ragavan K V, Thakur MS, Raghavarao KSMS. Recent advances in nanoparticle based aptasensors for food contaminants. Biosens Bioelectron 2015;74:612–27. doi:10.1016/j.bios.2015.07.017.

[31] Schindelin J, Arganda-Carreras I, Frise E, Kaynig V, Longair M, Pietzsch T, et al. Fiji:

an open-source platform for biological-image analysis. Nat Methods 2012;9:676–82. doi:10.1038/nmeth.2019.

[32] Yamaguchi M, Araga S, Mita M, Yamasaki K, Maekawa K. On-Demand Infrared Laser Sintering of Gold Nanoparticle Paste for Electrical Contacts. IEEE Trans Components, Packag Manuf Technol 2015;5:1160–8. doi:10.1109/TCPMT.2015.2450312.

[33] Ansari SA, Husain Q. Potential applications of enzymes immobilized on/in nano materials: A review. Biotechnol Adv 2012;30:512–23. doi:10.1016/j.biotechadv.2011.09.005.

[34] Huang X, El-Sayed MA. Gold nanoparticles: Optical properties and implementations in cancer diagnosis and photothermal therapy. J Adv Res 2010;1:13–28. doi:10.1016/j.jare.2010.02.002.

[35] Maye MM, Han L, Kariuki NN, Ly NK, Chan W Ben, Luo J, et al. Gold and alloy nanoparticles in solution and thin film assembly: Spectrophotometric determination of molar absorptivity. Anal Chim Acta 2003;496:17–27. doi:10.1016/S0003-2670(03)00986-3.

[36] McCann R, Bagga K, Groarke R, Stalcup A, Vázquez M, Brabazon D. Microchannel fabrication on cyclic olefin polymer substrates via 1064nm Nd:YAG laser ablation. Appl Surf Sci 2016;387:603–8. doi:10.1016/j.apsusc.2016.06.059.

[37] O'Neil CE, Taylor S, Ratnayake K, Pullagurla S, Singh V, Soper SA. Characterization of activated cyclic olefin copolymer: effects of ethylene/norbornene content on the physiochemical properties. Analyst 2016;141:6521–32. doi:10.1039/C6AN01448H.

[38] Stathaki T. Image Fusion: Algorithms and Applications. 1st ed. Elsevier; 2008.

[39] Gonzalez RC, Woods RE. Digital Image Processing. 3rd ed. Pearson; 2007.

[40] Voigtman E. Comparison of Signal-to-Noise Ratios. Anal Chem 1997;69:226–34. doi:10.1021/ac960675d.

[41] Patty A, Peijiang Z. Advances in Materials Sciences, Energy Technology and Environmental Engineering : Proceedings of the International Conference on Materials

Science, Energy Technology and Environmental Engineering, MSETEE 2016, Zhuhai, China, May 28-29, 2016. CRC Press; 2016.